Theory of light emission from a dipole source embedded in a chiral sculptured thin film

Tom G. Mackay[1*] **and Akhlesh Lakhtakia**[2]

[1]*School of Mathematics, University of Edinburgh, Edinburgh EH9 3JZ, United Kingdom*
[2]*Department of Engineering Science & Mechanics,*
Pennsylvania State University, University Park, PA 16802–6812
[*]*Corresponding author: T.Mackay@ed.ac.uk*

Abstract: Developing a theory based on a spectral Green function for light emission from a point–dipole source embedded in a chiral sculptured thin film (CSTF), we found that the intensity and polarization of the emitted light are strongly influenced by the structural handedness of the CSTF as well as the placement and orientation of the source dipole. The emission patterns across both pupils of the dipole–containing CSTF can be explained in terms of the circular Bragg phenomenon exhibited by CSTFs when illuminated by normally as well as obliquely incident plane waves. The emission characteristics augur well for the future of CSTFs as optical biosensors as well as light emitters with controlled circular polarization and bandwidth.

© 2007 Optical Society of America

OCIS codes: (310.6845) Thin films: Devices and applications; (310.6860) Thin films: Optical properties; (260.1440) Physical optics: Birefringence; (260.3800) Physical optics: Luminescence

References and links

1. A. Lakhtakia, R. Messier, M. J. Brett, and K. Robbie, "Sculptured thin films (STFs) for optical, chemical and biological applications," Innovations Mater. Res. **1**, 165176 (1996).
2. I. Hodgkinson and Q. h. Wu, "Inorganic chiral optical materials," Adv. Mater. **13**, 889–897 (2001).
3. A. Lakhtakia and R. Messier, *Sculptured Thin Films: Nanoengineered Morphology and Optics* (SPIE Press, Bellingham, WA, USA, 2005).
4. P. G. de Gennes and J. Prost, *The Physics of Liquid Crystals* (Oxford University Press, New York, NY, USA, 1993).
5. Q. Wu, I. J. Hodgkinson, and A. Lakhtakia, "Circular polarization filters made of chiral sculptured thin films: experimental and simulation results," Opt. Eng. **39**, 1863–1868 (2000).
6. I. J. Hodgkinson, Q. H. Wu, A. Lakhtakia, and M. W. McCall, "Spectral–hole filter fabricated using scultured thin–film technology," Opt. Commun. **177**, 79–84 (2000).
7. J. A. Polo Jr., "Sculptured thin films," in: *Micromanufacturing and Nanotechnology*, pp. 357–381, N. P. Mahalik, ed., Springer, Heidelberg, Germany (2005).
8. A. Lakhtakia, M. C. Demirel, M. W. Horn, and J. Xu, "Six emerging directions in sculptured–thin–film research," Adv. Solid State Phys. **46** (2008); in press.
9. R. Messier, V. C. Venugopal, and P. D. Sunal, "Origin and evolution of sculptured thin films," J. Vac. Sci. Technol. A **18**, 1538–1545 (2000).
10. A. Lakhtakia, "On bioluminescent emission from chiral sculptured thin films," Opt. Commun. **188**, 313–320 (2001).
11. H. Tan, O. Ezekoye, J. van der Schalie, M. W. Horn, A. Lakhtakia, J. Xu, and W. D. Burgos, "Biological reduction of nanoengineered iron III oxide sculptured thin films," Environ. Sci. Technol. **40**, 5490–5495 (2006).
12. S. Chan, Y. Li, L. J. Rothberg, B. L. Miller, and P. M. Fauchet, "Nanoscale silicon microcavities for biosensing," Mater. Sci. Eng. C **15**, 277–282 (2001).
13. L. De Stefano, I. Rendina, A. M. Rossi, M. Rossi, L. Rotiroti, and S. D'Auria, "Biochips at work: porous silicon microbiosensor for proteomic diagnostic," J. Phys.: Condens. Matter **19**, 395007 (2007).

#87251 - $15.00 USD Received 5 Sep 2007; revised 1 Oct 2007; accepted 1 Oct 2007; published 24 Oct 2007

14. K. Robbie, M. J. Brett, and A. Lakhtakia, "Chiral sculptured thin films," Nature **384**, 616 (1996).
15. P. C. P. Hrudey, K. L. Westra, and M. J. Brett, "Highly ordered organic Alq_3 chiral luminescent thin films fabricated by glancing–angle deposition," Adv. Mater. **18**, 224–228 (2006).
16. J. Xu, A. Lakhtakia, J. Liou, A. Chen, and I. J. Hodgkinson, "Circularly polarized fluorescence from light–emitting microcavities with sculptured–thin–film chiral reflectors," Opt. Commun. **264**, 235–239 (2006).
17. S. K. Arya, A. Chaubey, and B. D. Malhotra, "Fundamentals and applications of biosensors," Proc. Ind. Natn. Sci. Acad. **72**, 249–266 (2006).
18. A. Dorfman, N. Kumar, and J.–i. Hahm, "Highly sensitive biomolecular fluorescence detection using nanoscale ZnO platforms," Langmuir **22**, 4890–4895 (2006).
19. F. Zhang, J. Xu, A. Lakhtakia, S. M. Pursel, and M. W. Horn, "Circularly polarized emission from colloidal nanocrystal quantum dots confined in microcavities formed by chiral mirrors," Appl. Phys. Lett. **91**, 023102 (2007). [Interchange the labels LCP and RCP in Fig. 2c of this paper.]
20. B. Valeur, *Molecular Fluorescence: Principles and Applications* (Wiley–VCH, Weinheim, Germany, 2002).
21. A. Ishchenko, "Molecular engineering of dye–doped polymers for optoelectronics," Polym. Adv. Technol. **13**, 744–752 (2003).
22. F. Boxberg and J. Tulkki, "Quantum dots: Phenomenology, photonic and electronic properties, modeling and technology," in: *Nanometer Structures — Theory, Modeling, and Simulation*, pp. 107–143, A. Lakhtakia, ed., SPIE Press, Bellingham, WA, USA (2004).
23. A. Lakhtakia, "On radiation from canonical source configurations embedded in structurally chiral materials," Microwave Opt. Technol. Lett. **37**, 37–40 (2003).
24. M. P. C. M. Krijn, "Electromagnetic wave propagation in stratified anisotropic media in the presence of sources," Opt. Lett. **17**, 163–165 (1992). [Although Eq. (10) of this paper is not rigorously valid unless the matrix $\Delta(z)$ therein is either diagonal or independent of z, it can be useful with the piecewise uniform approximation technique provided a space–ordering operator is implemented on its right side [25].]
25. K. Eidner, "Light propagation in stratified anisotropic media: orthogonality and symmetry properties of the 4×4 matrix formalisms," J. Opt. Soc. Am. A **6**, 1657–1660 (1989).
26. A. Lakhtakia and W. S. Weiglhofer, "Green function for radiation and propagation in helicoidal bianisotropic mediums," IEE Proc.–Microw. Antennas Propag. **144**, 57–59 (1997).
27. A. Lakhtakia and M. W. McCall, "Response of chiral sculptured thin films to dipolar sources," Int. J. Electron. Commun. (AEÜ) **57**, 23–32 (2003).
28. D. W. Berreman, "Optics in stratified and anisotropic media: 4×4–matrix formulation," J. Opt. Soc. Am. **62**, 502–510 (1972).
29. M. Born and E. Wolf, *Principles of Optics*, Appendix III, 7th ed. (Pergamon, Oxford, UK, 1999).
30. F. Wang, "Note on the asymptotic approximation of a double integral with an angular–spectrum representation," Int. J. Electron. Commun. (AEÜ) **59**, 258–261 (2005).
31. F. Wang and A. Lakhtakia, "Response of slanted chiral sculptured thin films to dipolar sources," Opt. Commun. **235**, 133–151 (2004).
32. M. D. Pickett, A. Lakhtakia, and J. A. Polo Jr., "Spectral responses of gytrotropic chiral sculptured thin films to obliquely incident plane waves," Optik **9**, 393–398 (2004).
33. X.–H. Xu and A. J. Bard, "Immobilization and hybridization of DNA on an aluminum (III) alkanebisphophonate thin film with electrogenerated chemiluminescent detection," J. Am. Chem. Soc. **117**, 2627–2631 (1995).
34. W. Tabbara, V. Rannou, and S. Salio, "Statistical approaches to scattering," in: *Introduction to Complex Mediums for Optics and Electromagnetics*, pp. 591–608, W. S. Weiglhofer and A. Lakhtakia, eds., SPIE Press, Bellingham, WA, USA (2003).

1. Introduction

A chiral sculptured thin film (CSTF) is an assembly of parallel helical nanowires grown on a substrate by physical vapor deposition techniques [1, 2]. At optical wavelengths, a CSTF may be viewed as a unidirectionally nonhomogeneous continuum that locally possesses orthorhombic symmetry and globally is structurally chiral [3, Chap. 9]. Just like cholesteric liquid crystals [4], CSTFs also exhibit the circular Bragg phenomenon; i.e., a structurally right/left–handed CSTF of sufficient thickness almost completely reflects right/left–circularly polarized (RCP/LCP) light which is normally incident, but LCP/RCP light is reflected very little, within a wavelength regime called the Bragg regime. This phenomenon has been exploited to use CSTFs as circular polarization [5] and spectral–hole [6] filters, among other applications [7, 8].

The multiscale porosity [9] of CSTFs makes them highly promising platforms for optical sensing applications [10, 11]. Unlike porous–silicon platforms [12, 13], CSTFs can be used to generate and detect signals with a high degree of circular polarization and a narrow bandwidth

#87251 - $15.00 USD Received 5 Sep 2007; revised 1 Oct 2007; accepted 1 Oct 2007; published 24 Oct 2007
(C) 2007 OSA

[14, 15, 16]. This attribute is going to be significant for optical biosensors that exploit luminescence [17, 18], as well as for light–emitting devices with precise control over the circular polarization state and the emission wavelengths [19].

Photoluminescence and electroluminescence are common phenomenons wherein a material emits light in response to optical illumination and electrical excitation, respectively. These phenomenons underlie not only the commercial use of fluorescent tagging and identification techniques [20], phosphorescent dyes in displays, and dye–doped lasers [21], but are also responsible for the extraordinary interest of researchers in quantum dots these days [22]. Layers of quantum dots have indeed been inserted in CSTFs, and preliminary experiments have upheld the promise of quantum–dot–impregnated CSTFs as sources of circularly polarized light [16, 19].

These experimental results prompted us to continue the development of a theory of light emission from sources embedded in CSTFs. Earlier research had been confined to a transversely uniform distribution of sources that could emit light only normally with respect to the two pupils of a CSTF [10, 23]. In contrast, in this paper, we are concerned with emission from a single point–dipole source embedded in a CSTF. Light would then be emitted in all directions, which necessitates the use of a full–fledged spectral–Green–function formalism [24, 26].

The plan of this paper is as follows. Section 2 contains a detailed derivation of the theory of light emission by a point electric dipole embedded in a CSTF. Section 3 provides key numerical results that illustrate the chief features of light emitted by a dipole–containing CSTF, and discussions thereof. An $\exp(-i\omega t)$ time–dependence is implicit, with ω as the angular frequency; vectors are denoted in boldface, with the Cartesian unit vectors denoted by $\mathbf{u}_{x,y,z}$; dyadics are double–underlined; and column vectors as well as matrixes are denoted in boldface and enclosed within square brackets. The permittivity and the permeability of free space are denoted by ε_0 and μ_0, respectively; $k_0 = \omega\sqrt{\varepsilon_0\mu_0}$ is the free–space wavenumber; $\lambda_0 = 2\pi/k_0$ is the free–space wavelength; and $\eta_0 = \sqrt{\mu_0/\varepsilon_0}$ is the intrinsic impedance of free space.

2. Theory

The theory of planewave reflection and transmission involving a CSTF is comprehensively described elsewhere [3, Chap. 9]. It has been applied to develop a spectral–Green–function formalism for radiation inside a CSTF [26] as well as to investigate the shielding of a point–dipole source by a CSTF [27]. Here we extend these earlier treatments in order to accommodate radiation by a point–dipole source embedded inside a CSTF.

Suppose the region $-L \le z \le L$ is occupied by a CSTF whose frequency–domain constitutive relations are

$$\mathbf{D}(\mathbf{r},\omega) = \varepsilon_0 \underline{\underline{\varepsilon}}_r^{CSTF}(z,\omega)\cdot\mathbf{E}(\mathbf{r},\omega)\,, \qquad \mathbf{B}(\mathbf{r},\omega) = \mu_0\mathbf{H}(\mathbf{r},\omega)\,. \tag{1}$$

The relative permittivity dyadic of the CSTF is written in dyadic notation as [3, Chap. 9]

$$\underline{\underline{\varepsilon}}_r^{CSTF}(z,\omega) = \underline{\underline{S}}_z(z,h)\cdot\underline{\underline{S}}_y(\chi)\cdot\underline{\underline{\varepsilon}}_{ref}(\omega)\cdot\underline{\underline{S}}_y^{-1}(\chi)\cdot\underline{\underline{S}}_z^{-1}(z,h), \tag{2}$$

where

$$\underline{\underline{\varepsilon}}_{ref}(\omega) = \varepsilon_b(\omega)\,\mathbf{u}_x\mathbf{u}_x + \varepsilon_c(\omega)\,\mathbf{u}_y\mathbf{u}_y + \varepsilon_a(\omega)\,\mathbf{u}_z\mathbf{u}_z\,, \tag{3}$$

$$\underline{\underline{S}}_y(\chi) = (\mathbf{u}_x\mathbf{u}_x + \mathbf{u}_z\mathbf{u}_z)\cos\chi + (\mathbf{u}_z\mathbf{u}_x - \mathbf{u}_x\mathbf{u}_z)\sin\chi + \mathbf{u}_y\mathbf{u}_y\,, \tag{4}$$

$$\underline{\underline{S}}_z(z,h) = (\mathbf{u}_x\mathbf{u}_x + \mathbf{u}_y\mathbf{u}_y)\cos\left[h\frac{\pi(z+L)}{\Omega}\right] + (\mathbf{u}_y\mathbf{u}_x - \mathbf{u}_x\mathbf{u}_y)\sin\left[h\frac{\pi(z+L)}{\Omega}\right] + \mathbf{u}_z\mathbf{u}_z\,, \tag{5}$$

#87251 - $15.00 USD Received 5 Sep 2007; revised 1 Oct 2007; accepted 1 Oct 2007; published 24 Oct 2007
(C) 2007 OSA

with 2Ω being the pitch of the helical nanowires, χ the nanowire inclination angle with respect to the xy plane, and $h = \pm 1$ the structural handedness parameter. The regions $z < -L$ and $z > L$ are vacuous.

An electric dipole of moment $p/2$ and oriented in the direction of the unit vector $\mathbf{u}_J$ is embedded at $\mathbf{r} = d\,\mathbf{u}_z$, $-L < d < L$; hence, the source current density phasor

$$\mathbf{J}(\mathbf{r},\omega) = -\frac{i\omega p}{2}\,\mathbf{u}_J\,\delta(z-d)\,\delta(x)\,\delta(y)\,, \tag{6}$$

where $\delta(\cdot)$ is the Dirac delta function. In consonance with the spectral–Green–function formalism [26], we express $\mathbf{J}(\mathbf{r},\omega)$ as the spatial Fourier transform

$$\mathbf{J}(\mathbf{r},\omega) = \frac{1}{4\pi^2}\int_0^\infty d\kappa\,\kappa \int_0^{2\pi} d\psi\,\mathbf{j}(z,\kappa,\psi,\omega)\,\exp\left[i\kappa\left(x\cos\psi + y\sin\psi\right)\right], \tag{7}$$

wherein $\mathbf{j}(z,\kappa,\psi,\omega) = -(i\omega p/2)\,\mathbf{u}_J\,\delta(z-d)$ follows from (6). In order to describe the dipole orientation consistently with (2)–(5), we choose $\mathbf{u}_J \in \left\{\underline{\underline{S}}_z(d,h)\cdot\mathbf{u}_\tau, \underline{\underline{S}}_z(d,h)\cdot\mathbf{u}_n, \underline{\underline{S}}_z(d,h)\cdot\mathbf{u}_b\right\}$, where the unit vectors

$$\mathbf{u}_\tau = \mathbf{u}_x\cos\chi + \mathbf{u}_z\sin\chi\,, \quad \mathbf{u}_n = -\mathbf{u}_x\sin\chi + \mathbf{u}_z\cos\chi\,, \quad \mathbf{u}_b = -\mathbf{u}_y\,. \tag{8}$$

2.1. *Spectral Green function for fields inside the CSTF*

Let us now consider only a single spatial–Fourier component of $\mathbf{J}(\mathbf{r},\omega)$, i.e.,

$$\mathbf{J}(\mathbf{r},\kappa,\psi,\omega) = \mathbf{j}(z,\kappa,\psi,\omega)\,\exp\left[i\kappa\left(x\cos\psi + y\sin\psi\right)\right]. \tag{9}$$

In consonance with (9), the electromagnetic field phasors for $-L < z < L$ may be expressed as

$$\mathbf{E}(\mathbf{r},\kappa,\psi,\omega) = \mathbf{e}(z,\kappa,\psi,\omega)\,\exp\left[i\kappa\left(x\cos\psi + y\sin\psi\right)\right], \tag{10}$$

$$\mathbf{H}(\mathbf{r},\kappa,\psi,\omega) = \mathbf{h}(z,\kappa,\psi,\omega)\,\exp\left[i\kappa\left(x\cos\psi + y\sin\psi\right)\right]. \tag{11}$$

Substitution of the phasors (9)–(11) and constitutive relations (1) into the frequency–domain Maxwell curl postulates leads to:

(i) two algebraic equations which may be solved to find

$$\begin{aligned} e_z(z,\kappa,\psi,\omega) = \frac{1}{\varepsilon_a\cos^2\chi + \varepsilon_b\sin^2\chi}\Bigg(& (\varepsilon_a - \varepsilon_b)\sin\chi\,\cos\chi \\ & \times\left\{e_x(z,\kappa,\psi,\omega)\cos\left[h\frac{\pi(z+L)}{\Omega}\right] + e_y(z,\kappa,\psi,\omega)\sin\left[h\frac{\pi(z+L)}{\Omega}\right]\right\} \\ & + \frac{1}{\omega\varepsilon_0}\left\{\kappa\left[h_x(z,\kappa,\psi,\omega)\sin\psi - h_y(z,\kappa,\psi,\omega)\cos\psi\right] - i\,j_z(z,\kappa,\psi,\omega)\right\}\Bigg) \end{aligned} \tag{12}$$

and

$$h_z(z,\kappa,\psi,\omega) = -\frac{\kappa}{\omega\mu_0}\left[e_x(z,\kappa,\psi,\omega)\sin\psi - e_y(z,\kappa,\psi,\omega)\cos\psi\right]; \tag{13}$$

and

(ii) four ordinary differential equations which may be compactly expressed as

$$\begin{aligned} \frac{d}{dz}\left[\mathbf{f}(z,\kappa,\psi,\omega)\right] &= i\left[\mathbf{P}(z,\kappa,\psi,\omega)\right]\left[\mathbf{f}(z,\kappa,\psi,\omega)\right] \\ & \quad - \frac{i\omega p}{2}\delta(z-d)\left[\mathbf{g}(z,\kappa,\psi,\omega)\right], \quad z \in (-L,L)\,, \end{aligned} \tag{14}$$

#87251 - $15.00 USD Received 5 Sep 2007; revised 1 Oct 2007; accepted 1 Oct 2007; published 24 Oct 2007
(C) 2007 OSA

with the column vectors

$$[\mathbf{f}(z,\kappa,\psi,\omega)] = \begin{bmatrix} e_x(z,\kappa,\psi,\omega) \\ e_y(z,\kappa,\psi,\omega) \\ h_x(z,\kappa,\psi,\omega) \\ h_y(z,\kappa,\psi,\omega) \end{bmatrix} \tag{15}$$

and

$$[\mathbf{g}(z,\kappa,\psi,\omega)] = \frac{\mathbf{u}_J \cdot \mathbf{u}_z}{\varepsilon_a \cos^2\chi + \varepsilon_b \sin^2\chi} \begin{bmatrix} \frac{\kappa\cos\psi}{\omega\varepsilon_0} \\ \frac{\kappa\sin\psi}{\omega\varepsilon_0} \\ (\varepsilon_a-\varepsilon_b)\sin\chi\cos\chi\sin\left[h\frac{\pi(z+L)}{\Omega}\right] \\ (\varepsilon_b-\varepsilon_a)\sin\chi\cos\chi\cos\left[h\frac{\pi(z+L)}{\Omega}\right] \end{bmatrix} + \begin{bmatrix} 0 \\ 0 \\ \mathbf{u}_J \cdot \mathbf{u}_y \\ -\mathbf{u}_J \cdot \mathbf{u}_x \end{bmatrix}. \tag{16}$$

The 4×4 matrix $[\mathbf{P}(z,\kappa,\psi,\omega)]$ is straightforward to derive but too cumbersome to reproduce here; see [3, eqn. (9.116)]. Without the source term, (14) for unidirectionally nonhomogeneous mediums is often attributed to Berreman [28].

The solution of the matrix ordinary differential equation (14) is given as [24, 26]

$$\begin{aligned} [\mathbf{f}(z,\kappa,\psi,\omega)] &= [\mathbf{G}(z,-L,\kappa,\psi,\omega)]\,[\mathbf{f}(-L,\kappa,\psi,\omega)] \\ &\quad + \int_{-L}^{z} [\mathbf{G}(z,z_s,\kappa,\psi,\omega)]\,[\mathbf{g}(z_s,\kappa,\psi,\omega)]\; dz_s\,, \quad z\in[-L,L]\,. \end{aligned} \tag{17}$$

Herein the spectral Green function

$$[\mathbf{G}(z,z_s,\kappa,\psi,\omega)] = [\mathbf{M}(z,\kappa,\psi,\omega)]\,[\mathbf{M}(z_s,\kappa,\psi,\omega)]^{-1} \tag{18}$$

is given in terms of the 4×4 matrizant $[\mathbf{M}(z,\kappa,\psi,\omega)]$ which satisfies the matrix ordinary differential equation

$$\frac{d}{dz}[\mathbf{M}(z,\kappa,\psi,\omega)] = i\,[\mathbf{P}(z,\kappa,\psi,\omega)]\,[\mathbf{M}(z,\kappa,\psi,\omega)] \tag{19}$$

and the boundary condition $[\mathbf{M}(-L,\kappa,\psi,\omega)] = [\mathbf{I}]$, with $[\mathbf{I}]$ being the 4×4 identity matrix. The general solution (17) yields the particular solution

$$\begin{aligned} [\mathbf{f}(L,\kappa,\psi,\omega)] &= [\mathbf{M}(2L,\kappa,\psi,\omega)]\,[\mathbf{f}(-L,\kappa,\psi,\omega)] \\ &\quad + [\mathbf{M}(2L,\kappa,\psi,\omega)]\,[\mathbf{M}(d+L,\kappa,\psi,\omega)]^{-1}\,[\mathbf{g}(d,\kappa,\psi,\omega)] \end{aligned} \tag{20}$$

of (14). For computing the numerical results presented in Section 3, we adopted the piecewise uniform approximation technique [3, Chap. 9] to evaluate $[\mathbf{M}(2L,\kappa,\psi,\omega)]$ and $[\mathbf{M}(d+L,\kappa,\psi,\omega)]$.

2.2. *Boundary–value problem*

Light is emitted into the vacuous regions $z<-L$ and $z>L$ due to the source term (6). The electromagnetic field phasors for $z<-L$ may be expressed as

$$\begin{aligned} \mathbf{E}(\mathbf{r},\kappa,\psi,\omega) &= \frac{1}{\sqrt{2}}\left[-b_L(\kappa,\psi,\omega)(i\mathbf{s}-\mathbf{p}_-)+b_R(\kappa,\psi,\omega)(i\mathbf{s}+\mathbf{p}_-)\right] \\ &\quad \times\exp\left\{i\left[\kappa(x\cos\psi+y\sin\psi)-\alpha_0(z+L)\right]\right\}, \end{aligned} \tag{21}$$

$$\begin{aligned} \mathbf{H}(\mathbf{r},\kappa,\psi,\omega) &= \frac{i}{\eta_0\sqrt{2}}\left[b_L(\kappa,\psi,\omega)(i\mathbf{s}-\mathbf{p}_-)+b_R(\kappa,\psi,\omega),\omega(i\mathbf{s}+\mathbf{p}_-)\right] \\ &\quad \times\exp\left\{i\left[\kappa(x\cos\psi+y\sin\psi)-\alpha_0(z+L)\right]\right\}, \end{aligned} \tag{22}$$

#87251 - $15.00 USD Received 5 Sep 2007; revised 1 Oct 2007; accepted 1 Oct 2007; published 24 Oct 2007
(C) 2007 OSA

while those for $z > L$ may be expressed in similar terms as

$$\begin{aligned}\mathbf{E}(\mathbf{r},\kappa,\psi,\omega) &= \frac{1}{\sqrt{2}}\left[c_L(\kappa,\psi,\omega)(i\mathbf{s}-\mathbf{p}_+)-c_R(\kappa,\psi,\omega)(i\mathbf{s}+\mathbf{p}_+)\right] \\ &\quad\times\exp\left\{i\left[\kappa(x\cos\psi+y\sin\psi)+\alpha_0(z-L)\right]\right\}, \qquad (23)\\ \mathbf{H}(\mathbf{r},\kappa,\psi,\omega) &= -\frac{i}{\eta_0\sqrt{2}}\left[c_L(\kappa,\psi,\omega)(i\mathbf{s}-\mathbf{p}_+)+c_R(\kappa,\psi,\omega)(i\mathbf{s}+\mathbf{p}_+)\right] \\ &\quad\times\exp\left\{i\left[\kappa(x\cos\psi+y\sin\psi)+\alpha_0(z-L)\right]\right\}, \qquad (24)\end{aligned}$$

where $\alpha_0 = +\sqrt{k_0^2-\kappa^2}$. The scalars $b_L(\kappa,\psi,\omega)$ and $c_L(\kappa,\psi,\omega)$ are the amplitudes of the LCP components; $b_R(\kappa,\psi,\omega)$ and $c_R(\kappa,\psi,\omega)$ are the amplitudes of the RCP components; and the unit vectors

$$\mathbf{s} = -\mathbf{u}_x\sin\psi+\mathbf{u}_y\cos\psi, \quad \mathbf{p}_\pm = \mp(\alpha_0/k_0)(\mathbf{u}_x\cos\psi+\mathbf{u}_y\sin\psi)+(\kappa/k_0)\mathbf{u}_z \qquad (25)$$

delineate the s– and p–polarization states. The ω–dependences of $\mathbf{p}_\pm$ and α_o have not been explicitly identified here.

The boundary values

$$[\mathbf{f}(-L,\kappa,\psi,\omega)] = \frac{1}{\sqrt{2}}[\mathbf{K}(\kappa,\psi,\omega)]\begin{bmatrix}0\\0\\-i[b_L(\kappa,\psi,\omega)-b_R(\kappa,\psi,\omega)]\\b_L(\kappa,\psi,\omega)+b_R(\kappa,\psi,\omega)\end{bmatrix} \qquad (26)$$

and

$$[\mathbf{f}(L,\kappa,\psi,\omega)] = \frac{1}{\sqrt{2}}[\mathbf{K}(\kappa,\psi,\omega)]\begin{bmatrix}i[c_L(\kappa,\psi,\omega)-c_R(\kappa,\psi,\omega)]\\-[c_L(\kappa,\psi,\omega)+c_R(\kappa,\psi,\omega)]\\0\\0\end{bmatrix} \qquad (27)$$

emerge from the continuity of the tangential components of $\mathbf{E}(\mathbf{r},\kappa,\psi,\omega)$ and $\mathbf{H}(\mathbf{r},\kappa,\psi,\omega)$ across the pupils $z=-L$ and $z=L$, respectively, of the CSTF, with the 4×4 matrix

$$[\mathbf{K}(\kappa,\psi,\omega)] = \begin{bmatrix}-\sin\psi & -(\alpha_0/k_0)\cos\psi & -\sin\psi & (\alpha_0/k_0)\cos\psi\\ \cos\psi & -(\alpha_0/k_0)\sin\psi & \cos\psi & (\alpha_0/k_0)\sin\psi\\ -\eta_0^{-1}(\alpha_0/k_0)\cos\psi & \eta_0^{-1}\sin\psi & \eta_0^{-1}(\alpha_0/k_0)\cos\psi & \eta_0^{-1}\sin\psi\\ -\eta_0^{-1}(\alpha_0/k_0)\sin\psi & -\eta_0^{-1}\cos\psi & \eta_0^{-1}(\alpha_0/k_0)\sin\psi & -\eta_0^{-1}\cos\psi\end{bmatrix}. \qquad (28)$$

After substituting (26) and (27) into (20), the four amplitudes $b_{L,R}(\kappa,\psi,\omega)$ and $c_{L,R}(\kappa,\psi,\omega)$ can be determined by standard algebraic techniques.

2.3. *Emitted electromagnetic field phasors*

The spectral electromagnetic phasors $\mathbf{E}(\mathbf{r},\kappa,\psi,\omega)$ and $\mathbf{H}(\mathbf{r},\kappa,\psi,\omega)$ in both vacuous regions $z>L$ and $z<-L$ are delivered from (21)–(24). Inverting the spatial Fourier transform, we can find the emitted electromagnetic phasors

$$\mathbf{E}(\mathbf{r},\omega) = \frac{1}{4\pi^2}\int_0^\infty d\kappa\int_0^{2\pi} d\psi\ \kappa\mathbf{E}(z,\kappa,\psi,\omega)\exp\left[i\kappa(x\cos\psi+y\sin\psi)\right], \qquad (29)$$

$$\mathbf{H}(\mathbf{r},\omega) = \frac{1}{4\pi^2}\int_0^\infty d\kappa\int_0^{2\pi} d\psi\ \kappa\mathbf{H}(z,\kappa,\psi,\omega)\exp\left[i\kappa(x\cos\psi+y\sin\psi)\right] \qquad (30)$$

for $z\notin[-L,L]$.

#87251 - $15.00 USD Received 5 Sep 2007; revised 1 Oct 2007; accepted 1 Oct 2007; published 24 Oct 2007
(C) 2007 OSA

Let us choose the observation point $\mathbf{r}^{obs} \equiv \left(r^{obs}, \theta^{obs}, \psi^{obs}\right)$ (in a spherical coordinate system) to evaluate the emitted field phasors in the far zone in the two vacuous regions; i.e., in the limit $k_0|\mathbf{r}| \to \infty$. We find the asymptotic approximations [29, 30]

$$\mathbf{E}(\mathbf{r}^{obs}, \omega) \approx \frac{i\cos\theta^{obs}}{2\sqrt{2}\pi}\left[-b_L^{obs}\left(i\mathbf{s}^{obs} - \mathbf{p}_-^{obs}\right) + b_R^{obs}\left(i\mathbf{s}^{obs} + \mathbf{p}_-^{obs}\right)\right]\frac{\exp\left(ik_0\tilde{r}_-^{obs}\right)}{k_0\tilde{r}_-^{obs}}, \tag{31}$$

$$\mathbf{H}(\mathbf{r}^{obs}, \omega) \approx -\frac{\cos\theta^{obs}}{\eta_0 2\sqrt{2}\pi}\left[b_L^{obs}\left(i\mathbf{s}^{obs} - \mathbf{p}_-^{obs}\right) + b_R^{obs}\left(i\mathbf{s}^{obs} + \mathbf{p}_-^{obs}\right)\right]\frac{\exp\left(ik_0\tilde{r}_-^{obs}\right)}{k_0\tilde{r}_-^{obs}} \tag{32}$$

for $z^{obs} < -L$, and

$$\mathbf{E}(\mathbf{r}^{obs}, \omega) \approx \frac{i\cos\theta^{obs}}{2\sqrt{2}\pi}\left[c_L^{obs}\left(i\mathbf{s}^{obs} - \mathbf{p}_+^{obs}\right) - c_R^{obs}\left(i\mathbf{s}^{obs} + \mathbf{p}_+^{obs}\right)\right]\frac{\exp\left(ik_0\tilde{r}_+^{obs}\right)}{k_0\tilde{r}_+^{obs}}, \tag{33}$$

$$\mathbf{H}(\mathbf{r}^{obs}, \omega) \approx \frac{\cos\theta^{obs}}{\eta_0 2\sqrt{2}\pi}\left[c_L^{obs}\left(i\mathbf{s}^{obs} - \mathbf{p}_+^{obs}\right) + c_R^{obs}\left(i\mathbf{s}^{obs} + \mathbf{p}_+^{obs}\right)\right]\frac{\exp\left(ik_0\tilde{r}_+^{obs}\right)}{k_0\tilde{r}_+^{obs}} \tag{34}$$

for $z^{obs} > L$, where $b_{L,R}^{obs} \equiv b_{L,R}(\kappa^{obs}, \psi^{obs}, \omega)$, $c_{L,R}^{obs} \equiv c_{L,R}(\kappa^{obs}, \psi^{obs}, \omega)$, $\kappa^{obs} = k_0 \sin\theta^{obs}$, and $\tilde{r}_\pm^{obs} = |\mathbf{r}^{obs} \mp L\mathbf{u}_z|$. The approximations (31)–(34) are appropriate at distances far from the CSTF pupils but do not possess physical significance in the vicinity of $\theta^{obs} = \pi/2$ [29, 30].

The time–averaged Poynting vector, $\mathbf{P}(\mathbf{r}, \omega) = (1/2)\mathrm{Re}\left[\mathbf{E}(\mathbf{r}, \omega) \times \mathbf{H}^*(\mathbf{r}, \omega)\right]$, at the observation point $\mathbf{r}^{obs} = r^{obs}\,\hat{\mathbf{r}}^{obs}$ in the far zone is given approximately as

$$\mathbf{P}(\mathbf{r}^{obs}, \omega) \approx \begin{cases} \frac{1}{2\eta_0}\left(|b_L^{obs}|^2 + |b_R^{obs}|^2\right)\left(\frac{\cos\theta^{obs}}{2\pi k_0 \tilde{r}_-^{obs}}\right)^2 \hat{\mathbf{r}}^{obs}, & z^{obs} < -L \\ \frac{1}{2\eta_0}\left(|c_L^{obs}|^2 + |c_R^{obs}|^2\right)\left(\frac{\cos\theta^{obs}}{2\pi k_0 \tilde{r}_+^{obs}}\right)^2 \hat{\mathbf{r}}^{obs}, & z^{obs} > L \end{cases}. \tag{35}$$

3. Numerical results

In characterizing the light emitted from the dipole–containing CSTF, it is helpful to distinguish between LCP and RCP contributions to the time–averaged Poynting vector, because of the circular–polarization–discriminatory properties of CSTFs. Therefore, we introduce

$$\mathbf{P}_{LCP}(\mathbf{r}^{obs}, \omega) \approx \begin{cases} \frac{1}{2\eta_0}\left(|b_L^{obs}|^2\right)\left(\frac{\cos\theta^{obs}}{2\pi k_0 \tilde{r}_-^{obs}}\right)^2 \hat{\mathbf{r}}^{obs}, & z^{obs} < -L \\ \frac{1}{2\eta_0}\left(|c_L^{obs}|^2\right)\left(\frac{\cos\theta^{obs}}{2\pi k_0 \tilde{r}_+^{obs}}\right)^2 \hat{\mathbf{r}}^{obs}, & z^{obs} > L \end{cases} \tag{36}$$

and

$$\mathbf{P}_{RCP}(\mathbf{r}^{obs}, \omega) \approx \begin{cases} \frac{1}{2\eta_0}\left(|b_R^{obs}|^2\right)\left(\frac{\cos\theta^{obs}}{2\pi k_0 \tilde{r}_-^{obs}}\right)^2 \hat{\mathbf{r}}^{obs}, & z^{obs} < -L \\ \frac{1}{2\eta_0}\left(|c_R^{obs}|^2\right)\left(\frac{\cos\theta^{obs}}{2\pi k_0 \tilde{r}_+^{obs}}\right)^2 \hat{\mathbf{r}}^{obs}, & z^{obs} > L \end{cases}, \tag{37}$$

and characterize the light emitted from the CSTF in terms of the relative magnitudes

$$\mathscr{P}_j(\mathbf{r}^{obs}, \omega) = \frac{|\mathbf{P}_j(\mathbf{r}^{obs}, \omega)|}{\omega^2|p|^2} \times 10^{13}, \quad j \in \{LCP, RCP\}. \tag{38}$$

In addition, we introduce the real–valued parameters Γ_j, $j \in \{LCP, RCP\}$, computed as

$$\Gamma_j = 10^3 \int_{\theta^{obs}=\rho_1}^{\rho_2} d\theta^{obs} \int_{\psi^{obs}=0}^{2\pi} d\psi^{obs} \left(r^{obs}\right)^2 \sin\theta^{obs}\, \mathscr{P}_j(\mathbf{r}^{obs}, \omega), \quad j \in \{LCP, RCP\}, \tag{39}$$

#87251 - $15.00 USD Received 5 Sep 2007; revised 1 Oct 2007; accepted 1 Oct 2007; published 24 Oct 2007
(C) 2007 OSA

where $\rho_1 = 0$, $\rho_2 = 0.95\pi/2$ for $z^{obs} > L$, and $\rho_1 = \pi - (0.95\pi/2)$, $\rho_2 = \pi$ for $z^{obs} < -L$. Thus, Γ_{LCP} and Γ_{RCP} provide a measure of the rates of energy flow into the vacuous regions $z > L$ and $z < -L$.

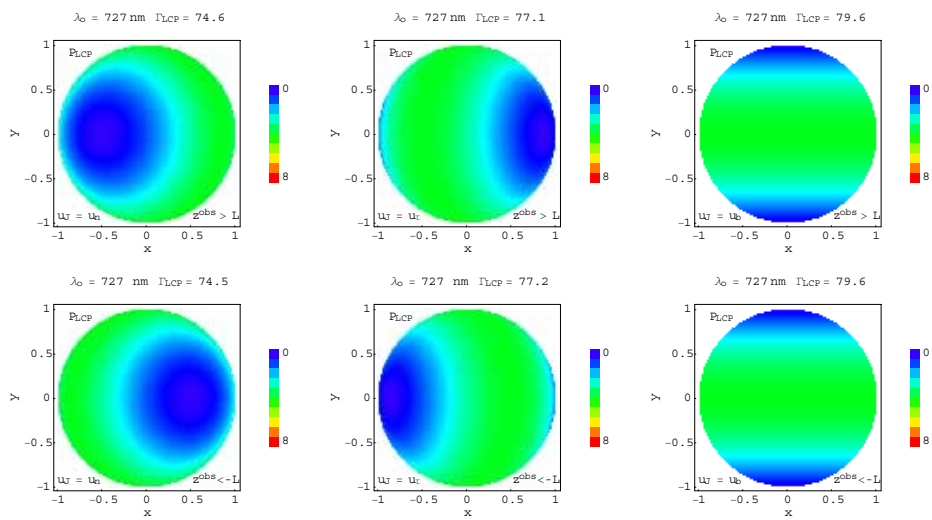

Fig. 1. Projections of $\mathscr{P}_{LCP}$ onto the $z = 0$ plane for the regions $z^{obs} > L$ (top row) and $z^{obs} < -L$ (bottom row), when $\underline{\underline{S}}_z^{-1}(d,h) \bullet \mathbf{u}_J \in \{\mathbf{u}_n, \mathbf{u}_\tau, \mathbf{u}_b\}$, $\lambda_0 = 727\,\text{nm}$, $d = 0$, and $\varepsilon_a = \varepsilon_b = \varepsilon_c = 1$.

A single–resonance Lorentzian model was selected for the relative permittivity scalars of the CSTF:

$$\varepsilon_{a,b,c} = 1 + \frac{q_{a,b,c}}{1 + \left(\frac{1}{N_{a,b,c}} - i\frac{\lambda_{a,b,c}}{\lambda_0}\right)^2}. \tag{40}$$

Here, $q_{a,b,c}$ are the oscillator strengths, while the parameters $\lambda_{a,b,c}$ and $N_{a,b,c}$ describe the resonance and absorption bands, respectively. We selected $q_a = 2.0$, $q_b = 2.6$, $q_c = 2.1$, $\lambda_a = \lambda_c = 180\,\text{nm}$, $\lambda_b = 150\,\text{nm}$ and $N_{a,b,c} = 500$. The structural parameters $\chi = 30^\circ$ and $\Omega = 200\,\text{nm}$ were chosen to ensure that the Bragg regime for normally incident plane waves is given by $702 \le \lambda_0 \le 752$ nm [31], while the thickness ratio $L/\Omega = 30$ was taken so that the circular Bragg phenomenon is fully developed. Also, we chose the CSTF to be structurally righ–handed ($h = +1$). For all calculations reported here, we chose the free–space wavelength $\lambda_0 \in \{652, 727, 802\}$ nm and the observation radius $r^{obs} = 10^5\lambda_0$.

Let us begin by considering a point–dipole source which lies midway through the CSTF ($d = 0$); accordingly, $\mathbf{u}_J \in \{\mathbf{u}_n, \mathbf{u}_\tau, \mathbf{u}_b\}$. In order to provide a reference for our numerical results, we initially converted the CSTF into free space by setting $\varepsilon_a = \varepsilon_b = \varepsilon_c = 1$. In Fig. 1, the projection of $\mathscr{P}_{LCP}$ is mapped onto the disc of radius r^{obs} (normalized to unity) in the $z = 0$ plane. The associated values of Γ_{LCP} are also indicated in Fig. 1. The data presented in Fig. 1 were obtained using $\lambda_0 = 727$ nm. The symmetry about the y axis but not about the x axis of the maps in the left and center columns of Fig. 1 indicates the tilted orientations of $\mathbf{u}_n$ and $\mathbf{u}_\tau$ relative to the x and z axes, whereas the fact that $\mathbf{u}_b$ lies along the y axis is clearly reflected in the symmetries of the maps about the x and the y axes in the right column of the same figure. The corresponding maps computed using $\lambda_0 = 652$ nm and 802 nm are indistinguishable from those in Fig. 1, because free space is nondispersive. Furthermore, the corresponding maps of $\mathscr{P}_{RCP}$ are indistinguishable from those in Fig. 1, because free space is isotropic and achiral.

#87251 - $15.00 USD Received 5 Sep 2007; revised 1 Oct 2007; accepted 1 Oct 2007; published 24 Oct 2007
(C) 2007 OSA

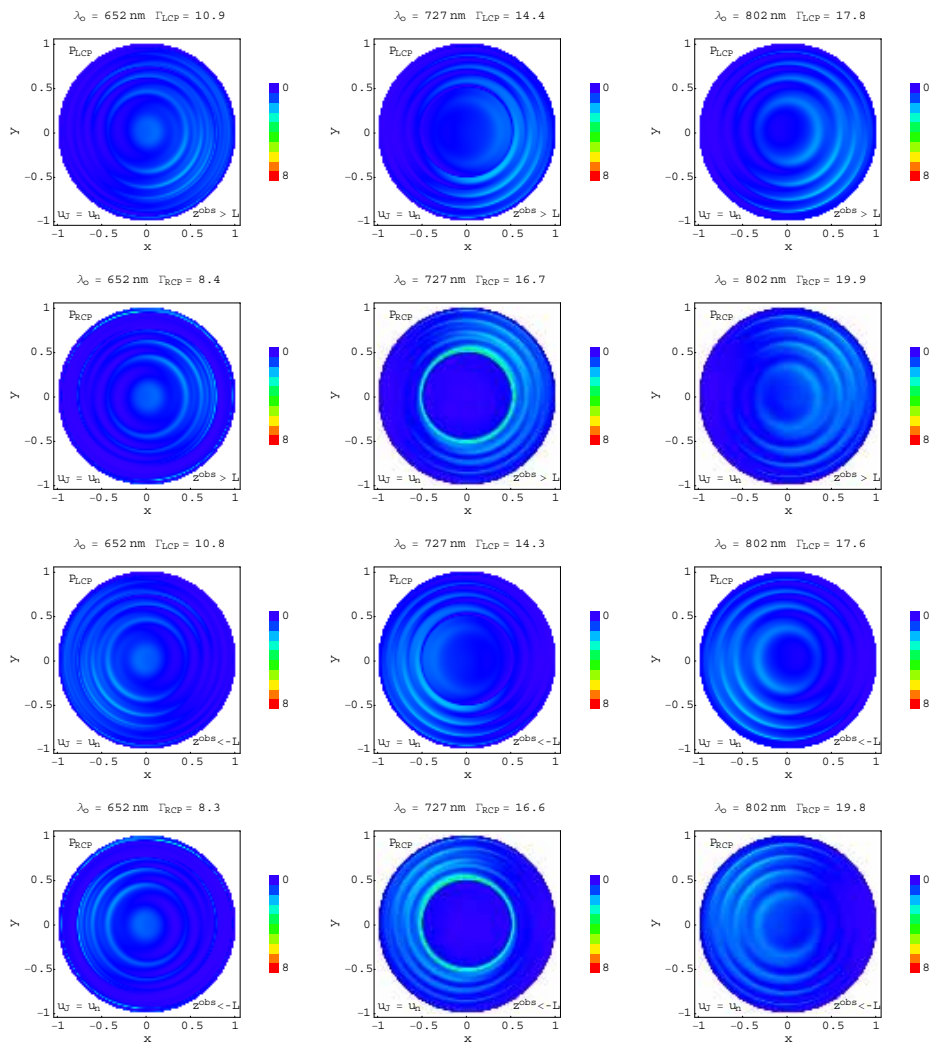

Fig. 2. Projections of $\mathscr{P}_{LCP}$ and $\mathscr{P}_{RCP}$ onto the $z=0$ plane for the regions $z^{obs}>L$ (top two rows) and $z^{obs}<-L$ (bottom two rows), when $\mathbf{u}_J = \underline{\underline{S}}_z(d,h)\bullet\mathbf{u}_n$, $\lambda_0 \in \{652,727,802\}$ nm and $h=1$. The relative permittivity parameters are prescribed by eqn. (40). The dipole source is located at $d=0$.

Let us now turn to the dipole embedded centrally in the CSTF. In Figs. 2, 3 and 4, the projections of $\mathscr{P}_{LCP}$ and $\mathscr{P}_{RCP}$ onto the $z=0$ plane are mapped for $\mathbf{u}_J=\mathbf{u}_n$, $\mathbf{u}_\tau$, and $\mathbf{u}_b$, respectively. The values of Γ_{LCP} and Γ_{RCP} are provided for each map, as appropriate. The following symmetries were analytically deduced for these maps and were supported by visual examination of specific features therein:

(i) $b^{obs}_{L,R}(\kappa^{obs},\psi^{obs}) = -b^{obs}_{L,R}(-\kappa^{obs},\psi^{obs}+\pi)$ and $c^{obs}_{L,R}(\kappa^{obs},\psi^{obs}) = -c^{obs}_{L,R}(-\kappa^{obs},\psi^{obs}+\pi)$ for $\mathbf{u}_J=\mathbf{u}_n$, $\mathbf{u}_\tau$, and $\mathbf{u}_b$;

(ii) $b^{obs}_{L,R}(\kappa^{obs},\psi^{obs}) = c^{obs}_{L,R}(-\kappa^{obs},-\psi^{obs})$ for $\mathbf{u}_J=\mathbf{u}_n$ and $\mathbf{u}_\tau$; and

(iii) $b^{obs}_{L,R}(\kappa^{obs},\psi^{obs}) = -c^{obs}_{L,R}(-\kappa^{obs},-\psi^{obs})$ for $\mathbf{u}_J=\mathbf{u}_b$.

#87251 - $15.00 USD Received 5 Sep 2007; revised 1 Oct 2007; accepted 1 Oct 2007; published 24 Oct 2007
(C) 2007 OSA

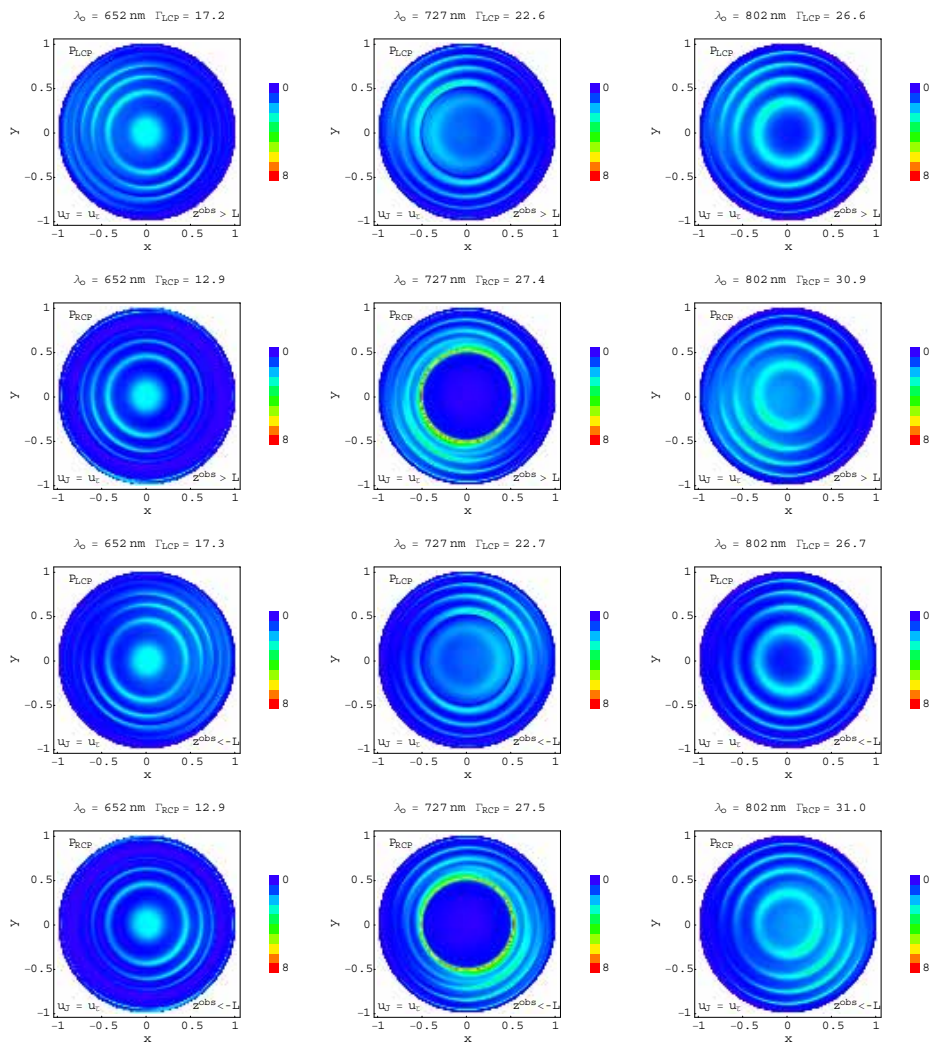

Fig. 3. As Fig. 2 but with $\mathbf{u}_J = \underline{\underline{S}}_z(d,h) \cdot \mathbf{u}_\tau$.

On comparing the values of Γ_{LCP} and Γ_{RCP} in Figs. 2–4 with those in Fig. 1, it is clear that the CSTF is a load on the dipole source; i.e., the dipole embedded in the CSTF is a less efficient emitter than the dipole in free space.

There are significant differences between the LCP and the RCP emission patterns in Figs. 2–4: Firstly, when $|\cos\theta^{obs}| \simeq 1$ (i.e., either normal or almost normal to the two pupils of the CSTF), these differences are more obvious for $\lambda_0 = 727$ nm than for $\lambda_0 = 652$ nm and 802 nm. This can be explained by the circular Bragg phenomenon for normally incident plane waves. Being structurally right–handed, the CSTF preferentially reflects normally incident RCP light for $\lambda_0 \in [702, 752]$ nm. Experimental data reported in Figs. 3a and 3b of Zhang *et al.* [19] for a CSTF with a central layer of quantum dots indicate that our dipole–containing CSTF must then be a preferential emitter of LCP light in the same wavelength regime. Secondly, when $0.4 < |\cos\theta_{obs}| < 0.8$ the difference between the LCP and the RCP emission patterns

#87251 - $15.00 USD Received 5 Sep 2007; revised 1 Oct 2007; accepted 1 Oct 2007; published 24 Oct 2007
(C) 2007 OSA

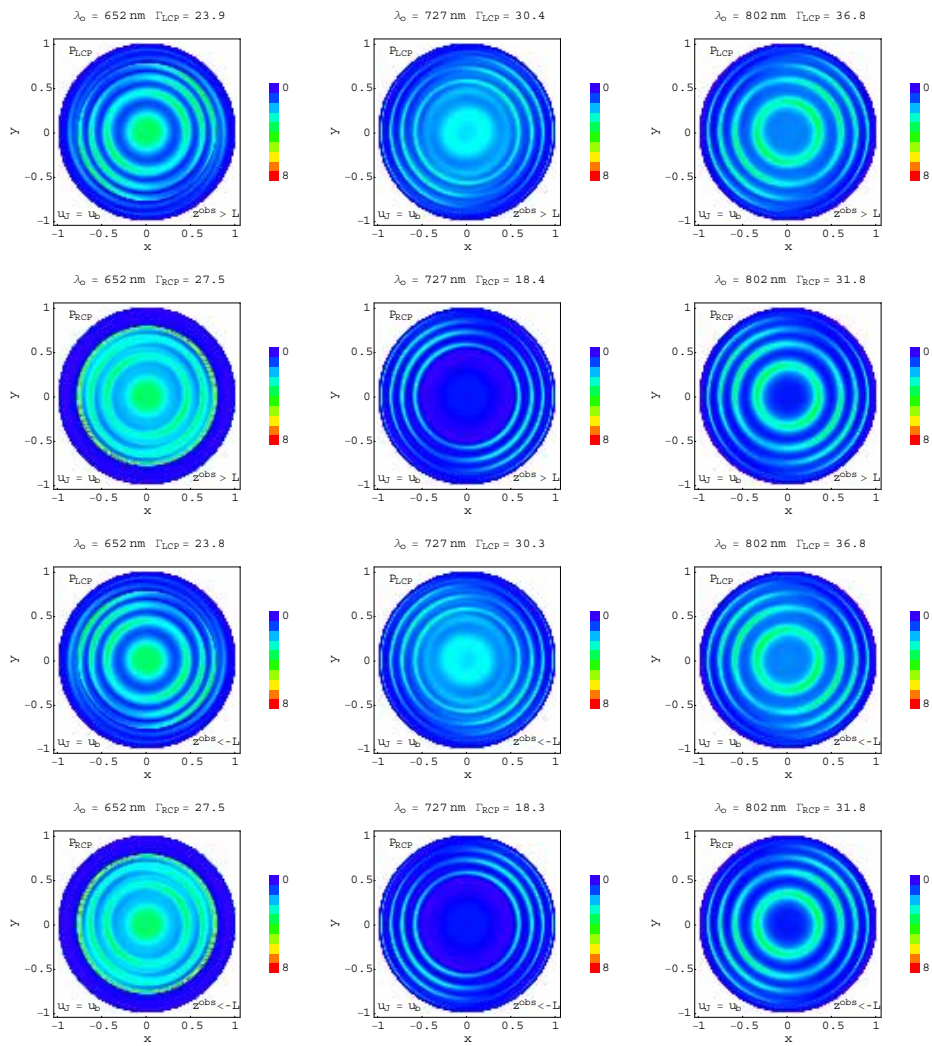

Fig. 4. As Fig. 2 but with $\mathbf{u}_J = \underline{\underline{S}}_z(d,h) \bullet \mathbf{u}_b$.

is more obvious for $\lambda_0 = 652$ nm than for $\lambda_0 = 727$ nm and 802 nm. This is indicative of the blueshift of the circular Bragg phenomenon for obliquely incident plane waves [3]. Thirdly, when $|\cos\theta_{obs}| < 0.4$, the distinction between the LCP and RCP patterns is very little, if any, for all three wavelengths. This reflects the huge diminishment of the circular Bragg phenomenon for highly oblique planewave incidence [32].

A notable feature of Figs. 2–4 is the presence of emission rings. In order to take account of the resonant effects of the CSTF pupils $z = -L$ and $z = L$, we repeated the computations for these figures, but with the CSTF replaced by an isotropic film of relative permittivity that is the arithmetic mean of ε_a, ε_b, and ε_c of (40). As is the case for Figs. 2–4, the dipole source was still located at $d = 0$. Plots of the projections of $\mathscr{P}_{LCP}$ onto the $z = 0$ plane, and the corresponding values of Γ_{LCP}, are provided in Fig. 5 for $\mathbf{u}_J = \mathbf{u}_n$, $\mathbf{u}_\tau$, and $\mathbf{u}_b$ at the free–space wavelength $\lambda_0 = 727$ nm. The corresponding plots of $\mathscr{P}_{RCP}$ are identical to those presented in

#87251 - $15.00 USD Received 5 Sep 2007; revised 1 Oct 2007; accepted 1 Oct 2007; published 24 Oct 2007
(C) 2007 OSA

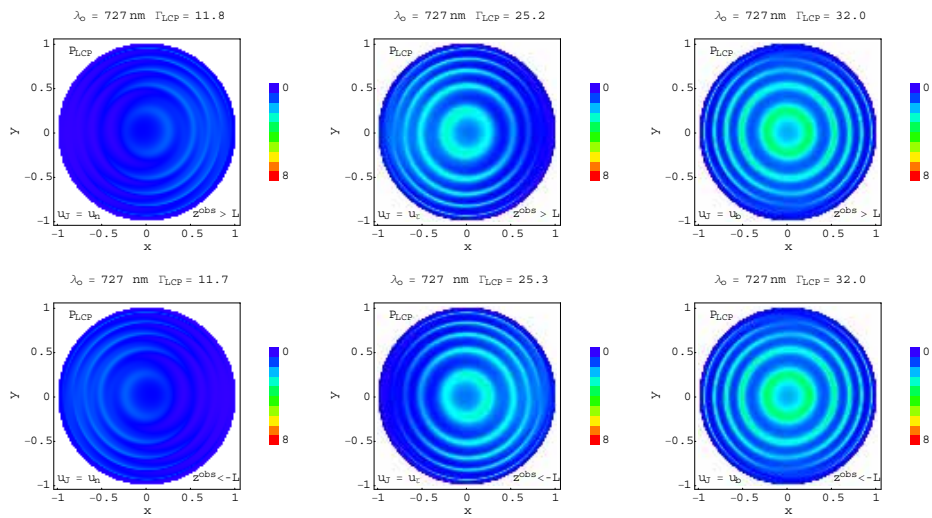

Fig. 5. Projections of $\mathscr{P}_{LCP}$ onto the $z=0$ plane for the reqions $z^{obs}>L$ (top row) and $z^{obs}<-L$ (bottom row), when $\underline{\underline{S}}_z(d,h)\cdot\mathbf{u}_J\in\{\mathbf{u}_n,\mathbf{u}_\tau,\mathbf{u}_b\}$, $\lambda_0=727\,\text{nm}$ and $h=1$. The CSTF has been replaced by an isotropic material with relative permittivity that is the arithmetic mean of ε_a, ε_b, and ε_c of eqn. (40). The dipole source is located at $d=0$.

Fig. 5 because the isotropic film is structurally achiral, and are therefore not displayed here. The annular emission features apparent in Fig. 5 have the same spatial frequency as those observed in Figs. 2–4. We infer that these are Fabry–Perot rings arising due to thickness resonances of the CSTF. The modulation of the Fabry–Perot ring pattern by the structural handedness of the CSTF can be deduced from Figs. 2–4.

Finally, we considered a dipole source located very close to the $z=L$ pupil of the CSTF; we set $d=L-40$ nm. The corresponding projections of $\mathscr{P}_{LCP}$ and $\mathscr{P}_{RCP}$ onto the $z=0$ plane are plotted in Figs. 6, 7 and 8, for $\mathbf{u}_J=\underline{\underline{S}}_z(d,h)\cdot\mathbf{u}_n$, $\underline{\underline{S}}_z(d,h)\cdot\mathbf{u}_\tau$, and $\underline{\underline{S}}_z(d,h)\cdot\mathbf{u}_b$, respectively. Asymmetries between the emission intensities through the closer and the distant pupils are highly conspicuous. In particular, we observe that in the Bragg regime, RCP light is preferentially emitted through the pupil closer to the source ($z=L$), whereas LCP light is preferentially emitted through the pupil farther from the source ($z=-L$). Also, light is generally emitted with greater intensity than for the symmetrically placed dipole source.

The effects of the location and orientation of a point source will become crucial when numerous point sources are embedded in a CSTF, e.g., by dispersing quantum dots [16, 19] or DNA fragments [33] in a CSTF, which are later excited optically, electrically, or chemically to emit light. The presented formalism is robust enough for theoretical examinations of such problems, when the interactions between the individual sources are sufficiently small to be ignored, and can also be used to develop a statistical understanding [34] after studying emission due to different ensembles of sources.

4. Closing remarks

Light emitted from a CSTF containing a point–dipole source bears the signatures of the structural handedness of the CSTF as well as the location and orientation of the source. Specifically, the emitted radiation can be circularly polarized to a high degree within the wavelength regime of the circular Bragg phenomenon relevant to directions offset from the direction normal to the

#87251 - $15.00 USD Received 5 Sep 2007; revised 1 Oct 2007; accepted 1 Oct 2007; published 24 Oct 2007
(C) 2007 OSA

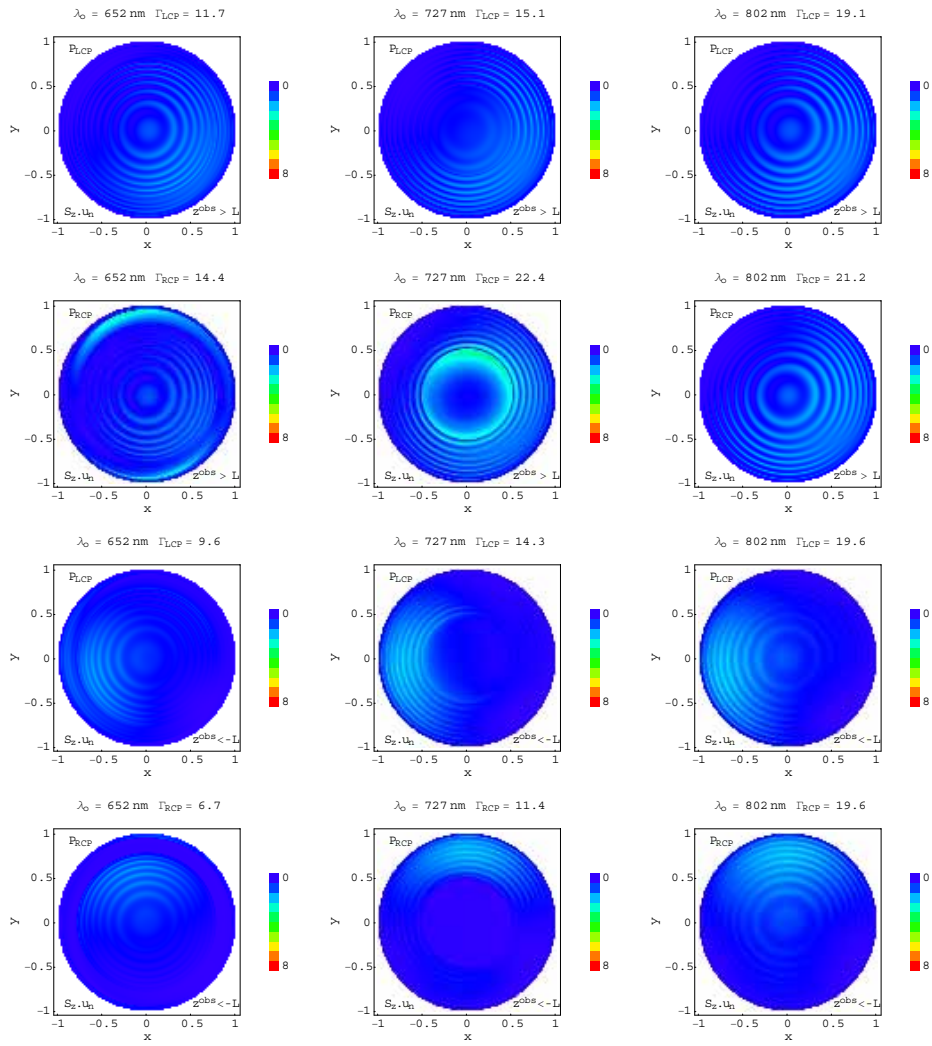

Fig. 6. Projections of $\mathscr{P}_{LCP}$ and $\mathscr{P}_{RCP}$ onto the $z=0$ plane for the regions $z^{obs} > L$ (top two rows) and $z^{obs} < -L$ (bottom two rows), when $\mathbf{u}_J = \underline{\underline{S}}_z(d,h) \bullet \mathbf{u}_n$, $\lambda_0 \in \{652, 727, 802\}$ nm and $h = 1$. The relative permittivity parameters are prescribed by eqn. (40). The dipole source is located at $d = L - 40$ nm.

#87251 - $15.00 USD Received 5 Sep 2007; revised 1 Oct 2007; accepted 1 Oct 2007; published 24 Oct 2007
(C) 2007 OSA

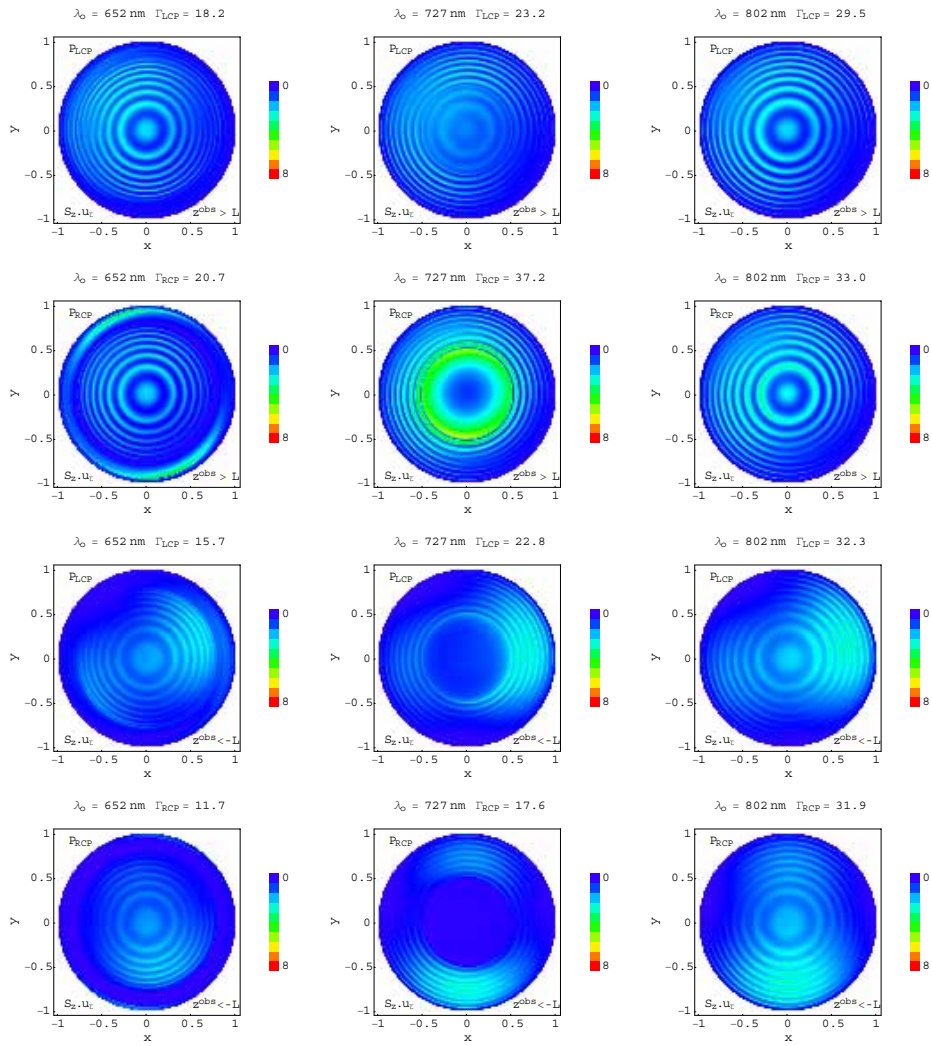

Fig. 7. As Fig. 6 but with $\mathbf{u}_J = \underline{\underline{S}}_z(d,h) \cdot \mathbf{u}_\tau$.

#87251 - $15.00 USD Received 5 Sep 2007; revised 1 Oct 2007; accepted 1 Oct 2007; published 24 Oct 2007
(C) 2007 OSA

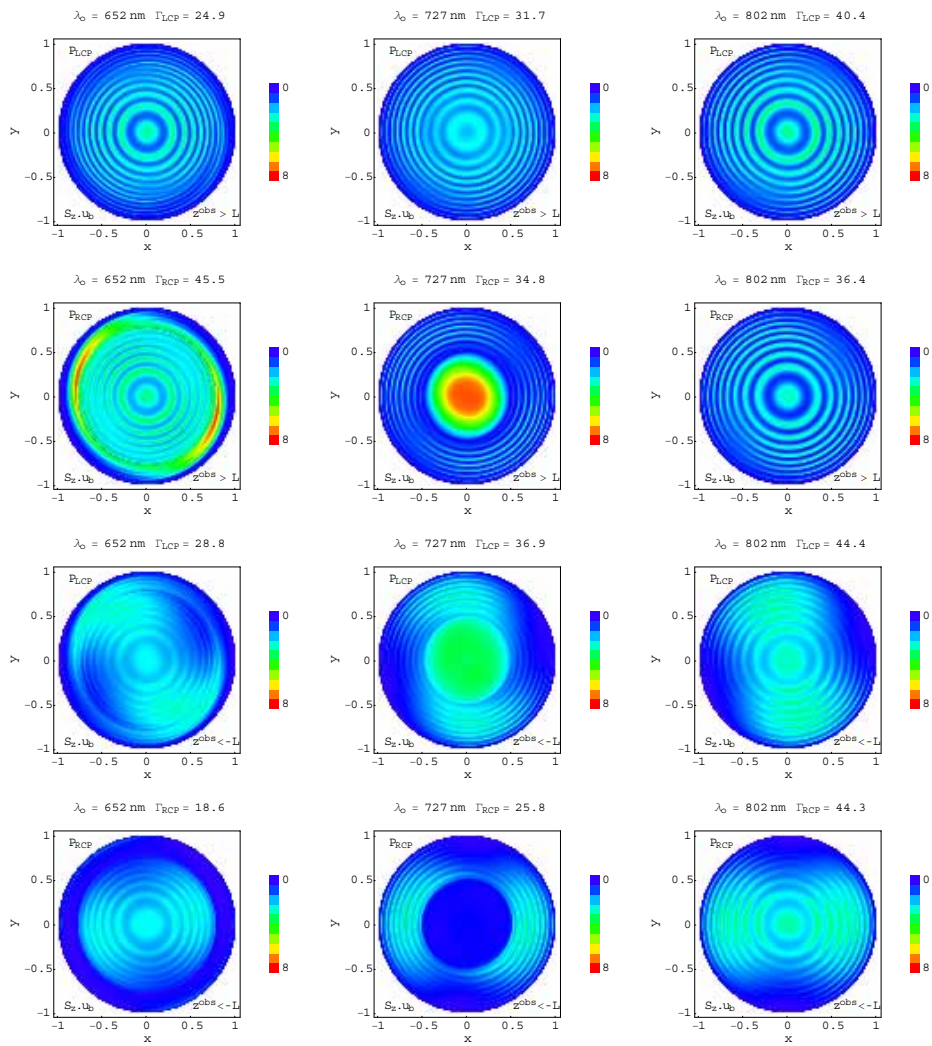

Fig. 8. As Fig. 6 but with $\mathbf{u}_J = \underline{\underline{S}}_z(d,h) \cdot \mathbf{u}_b$.

two pupils; the nature of circular polarization depends on the orientation and location of the dipole source. These emission characteristics augur well for the future development of CSTFs as platforms for optical sensing devices such as genomic sensors [8, 10, 33] as well as for light emitters with controlled circular polarization and bandwidth [15, 16, 19]. Accordingly, we will apply the developed theory to study emission characteristics of a CSTF containing monolayer and volumetric distributions of point–dipole sources, and eventually develop an integral–equation formalism for light emission from an arbitrary source embedded in a CSTF.

Acknowledgment

TGM is supported by a Royal Society of Edinburgh/Scottish Executive Support Research Fellowship. AL is supported in part by the Charles Godfrey Binder Endowment.